

Rotor Lattice Model of Ferroelectric Large Polarons

Georgios M. Koutentakis, Areg Ghazaryan, and Mikhail Lemesko

Institute of Science and Technology Austria (ISTA), am Campus 1, 3400 Klosterneuburg, Austria

(Dated: January 25, 2023)

We present a minimal model of charge transport in hybrid perovskites, which provides an intuitive explanation for the recently proposed formation of ferroelectric large polarons. We demonstrate that short-ranged charge-rotor interactions lead to long-range ferroelectric ordering of rotors, which strongly affects the carrier mobility. In the nonperturbative regime, where our theory cannot be reduced to any of the earlier models, we predict polaron properties in good agreement with experiment. This shows the potential of simple models to reveal electronic properties of molecular materials.

Hybrid organic-inorganic perovskites (HOIP) are praised for their outstanding performance as a building block of solar cells due to their long carrier lifetimes and diffusion lengths [1–3]. After the initial reports on spectacular optoelectronic properties of HOIP solar cells [4–7], the field has expanded at an unprecedented pace [8, 9]. It turned out, however, that HOIP are also notoriously complex in terms of their physical properties, *inter alia* due to their soft structure [10], ionic mobility [11, 12], and the interplay between cation rotational dynamics and structural, (photo)electric and stability properties of HOIP [13–16]. Recently a lot of progress has been made in theoretical understanding of HOIP using density functional theory [17–20], molecular dynamics [21] and machine learning [22–24] approaches. Based on atomistic simulations it is, however, challenging to achieve a simple intuitive understanding independent of the microscopic details, which motivates us to look for a simple model capturing the key physical properties of HOIP. Here we develop a one-dimensional rotor lattice model of charge carrier transport, which gives intuitive understanding to the recently proposed formation of a large polaron at ferroelectric domain boundaries [25–27].

Perhaps the most pressing issue to be addressed in HOIP is their charge transport properties. Earlier theories tried to explain it through screening of excitons by collective orientation of organic cations [28] and through modification of the band edges due to spin-orbit coupling induced by the cation through structural variability [17, 29, 30]. Interestingly, although the large recombination lifetimes and high diffusion lengths of HOIP are comparable to conventional semiconductors such as GaAs, the carrier mobilities in HOIP are orders of magnitude smaller [31]. This makes the issue even more puzzling and therefore, recent theories emphasize the role of the large polaron formation that screens the carriers from one another leading to longer carrier lifetimes [25–27, 32–39]. Despite that the detailed origin of large polaron formation is still debated. One recent approach [26, 27] is based on the formation of ferroelectric nanodomains and localization of electrons and holes in spatially separated regions. Charge carriers form ferroelectric large polarons in the direction of the domain wall and small polaron

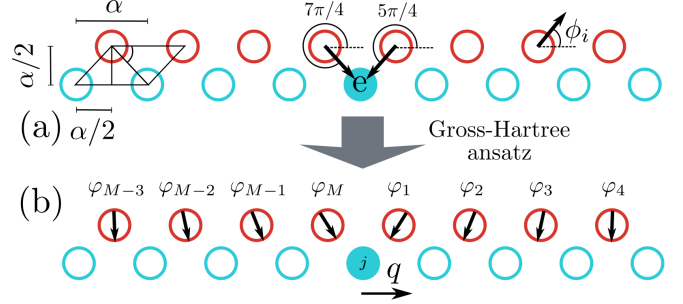


FIG. 1. (a) The tight binding model. Blue empty (filled) circles label empty (occupied) electron sites. Red circles show the dipole positions modeled by planar rotors. The distances between the sites and the orientations of the rotors/dipoles are also shown. (b) Illustration of the Gross-Hartree ansatz. The electron possesses quasimomentum, q , while the rotor states relative to it are described by the single-rotor states, $\varphi_j(\phi)$. Arrows show the orientations of the rotors.

perpendicular to it. The large polaron is characterized by fast coherent transport, whereas small polarons are characterized by slower hopping dynamics. This picture can explain the apparent contradicting features of HOIP, immunity of carriers to charge defects and the observed long diffusion lengths due to the large polaron and modest mobilities due to the small polarons. The molecular dynamics approach makes it, however, challenging to achieve a detailed understanding of the underlying mechanisms and their parametric dependence.

In this Letter we show that the formation of ferroelectric large polarons already takes place in a minimal model, where charge carriers interact with a one-dimensional array of planar rotors, see Fig. 1. The dipolar rotors model the reorientation dynamics of organic molecular cations, A^+ in the ABX_3 perovskite structure. Molecules interact with charge carriers hopping on the inorganic sublattice made of octahedral BX_6^- cages. Due to screening, we assume the charge-dipole interactions to be short-ranged [40]. As we show in what follows, the model captures the formation of local ferroelectric order and the crossover between the large-polaron (associated with ferroelectrically polarized dipoles) and the small-polaron regime characterized by charge carrier localiza-

tion at the boundary of two missaligned ferroelectrically ordered domains. This ferroelectric order strongly reduces the mobility of the carriers even within the large polaron regime, providing an avenue to obtain large diffusion length even when the mobility of carrier is significantly diminished.

The structure of our model is schematically shown in Fig. 1(a). Here the dipole and electron lattices are parallel to each other, have the same lattice spacing, α , and are offset by $\alpha/2$ in the direction along the lattice and a perpendicular one. The dipole reorientation dynamics are modeled by rigid planar rotors (in what follows we will use the terms dipoles and rotors interchangeably). We consider the case where each dipole interacts only with the electron on the neighboring sites, and there is no dipole–dipole interactions. The Hamiltonian of the model is given by

$$\begin{aligned} \hat{H} = & -t \sum_{i=1}^M (\hat{a}_{i+1}^\dagger \hat{a}_i + \text{h.c.}) - B \sum_{i=1}^M \frac{\partial^2}{\partial \phi_i^2} \\ & + V_0 \sum_{i=1}^M \hat{a}_i^\dagger \hat{a}_i \cos\left(\phi_i - \frac{\pi}{4}\right) \\ & + V_0 \sum_{i=2}^{M+1} \hat{a}_i^\dagger \hat{a}_i \cos\left(\phi_{i-1} - \frac{3\pi}{4}\right), \end{aligned} \quad (1)$$

where \hat{a}_i (\hat{a}_i^\dagger) are the electron annihilation (creation) operators, angles ϕ_i define the dipole orientations, t is the tunneling rate of the electron, B is the rotational constant of the dipoles, V_0 is the electron–dipole interaction strength and M is the number of rotors in the lattice. Note that herewith we employ periodic boundary conditions, i.e. $\hat{a}_{M+j}^\dagger = \hat{a}_j^\dagger$ for all $j = 1, \dots, M$. The model can be trivially extended to hole carriers by assuming $V_0 < 0$, nevertheless, here we consider only the case of electrons, $V_0 > 0$.

In HOIP the rotational energy of the molecule $B \sim 1$ meV is the lowest energy scale of the system since $V_0, t \sim 0.1 - 1$ eV [41]. To generate an appropriate rotor basis for $B \ll t$, we variationally optimize the state of the rotors relative to the electron, $\varphi_j(\phi)$, see Fig. 1(b). In particular we employ the following ansatz for the system’s wavefunction:

$$|\Psi_q(\phi_1, \dots, \phi_M)\rangle = \sum_{j=1}^M \frac{e^{i\frac{2\pi q j}{M}}}{\sqrt{M}} \prod_{k=1}^M \varphi_{I(k,j)}(\phi_k) \hat{a}_j^\dagger |0\rangle \quad (2)$$

where $|0\rangle$ and \hat{a}_j are the electron vacuum and creation operators and $q = 0, \dots, M - 1$ gives the quasimomentum of the polaron state. We will herewith refer to this approach as the variational Gross-Hartree method (vGH). The indices of $\varphi_j(\phi)$ appearing in Eq. (2) read $I(k, j) = 1 + [(M + k - j) \bmod M]$ and are selected such that the rotor state depends only on the relative distance between the rotor and the electron. For instance,

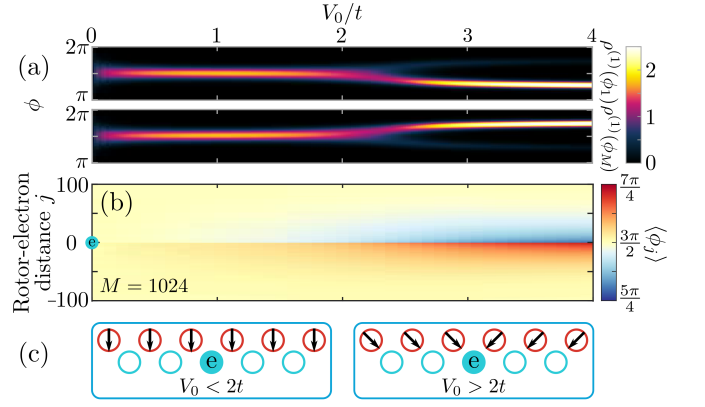


FIG. 2. (a) Single-rotor densities, $\rho^{(1)}(\phi_j)$, for $j = 1$ and $j = M$, as a function of the electron–rotor interaction, V_0 . The electron is fixed at the first site and $M = 4$. (b) Average rotor orientation, $\langle \phi_j \rangle$, depending on the electron–rotor interaction and V_0 for the case of $M = 1024$. In both cases $B = 10^{-3}t$. (c) Schematic illustration of the involved phases.

$\varphi_1(\phi)$ and $\varphi_M(\phi)$ refer to the state of the rotor on the right and left of the electron, respectively, independently of the position of the latter, cf. Fig. 1(b). Note that while the ansatz of Eq. (2) generalizes the well-known single-rotor basis generated via the Lang-Firsov transformation [42, 43] as it allows for t -dependent modifications of the rotor state, it neglects dipole–dipole correlations. This approximation can be shown to be adequate for our purposes by direct comparisons between vGH and exact diagonalization approaches for small M [44].

The order emerging in the rotor lattice can be elucidated by considering the single-rotor density at position j relative to the electron, $\rho^{(1)}(\phi_j) = |\varphi_j(\phi)|^2$, as shown in Fig. 2(a) for a small system with $M = 4$. In Fig. 2(b) we provide the average polarization of the rotors, $\langle \phi_j \rangle = \frac{3\pi}{2} + \int_{\pi/2}^{5\pi/2} d\phi_j \left(\phi_j - \frac{3\pi}{2}\right) \rho^{(1)}(\phi_j)$ for a large system of $M = 1024$, large enough to achieve convergence towards the $M \rightarrow \infty$ limit.

In the case of small $B = 10^{-3}t$, relevant for HOIP, we observe the emergence of two distinct interaction regimes. For $V_0 < 2t$ the rotors become strongly polarized towards the electronic lattice, $\phi \approx 3\pi/2$, and an almost perfect ferroelectric order emerges (see the left panel of Fig. 2(c)). Similarly, Fig. 2(b) shows $\langle \phi_j \rangle \approx 3\pi/2$ within this V_0 range. For $V_0 > 2t$, on the other hand, we observe domain formation in the rotor system, see the right panel of Fig. 2(c). The rotors to the left of the electron, $M/2 < j \leq M$, polarize with $\phi \approx 5\pi/4$, while the rotors at $1 \leq j \leq M/2$ polarize towards $\phi \approx 7\pi/4$. Thus, in this regime, the electron acts as a ferroelectric domain wall, with rotors on each side of the electron pointing towards it. From Fig. 2(b) we can see that although the rotor ordering is local, it is quite extensive and involves ~ 50 rotors in each side of the electron. Note that this change in ferroelectric order with varying V_0 is gradual, of typical crossover character [45, 46], as the rotors neighbour-

ing the electron from either side possess slightly different average polarizations even for $V_0 < 2t$, see Fig. 2(b).

The interaction dependence of the local ferroelectric order provides an intuitive picture for the role of molecular dipole moments in the formation of polarons at ferroelectric domain boundaries, as suggested in Ref. [27]. Indeed, in that work it is proposed that the carriers in HOIP are confined to move within a two-dimensional ferroelectric domain-wall with the hopping perpendicular to it being much slower due to the distortion of the inorganic lattice. In our model, this distortion can be thought of as a reduction of the tunnelling along the distortion direction, resulting in an effectively higher V_0/t that can exceed the threshold for formation of ferroelectric domain walls for the rotors, which is $V_0 \approx 2t$ in the one-dimensional case. In contrast, along the directions where no such distortion takes place, V_0/t remains smaller owing to the larger t , which according to our model stabilizes an almost perfectly polarized rotor state.

The origin of the emerging order can be elucidated by examining the polaron energy, E_0 , shown in Fig. 3(a), and its scaling with V_0/t , Fig. 3(b), and with B/t , Fig. 3(c). First, let us analyze the scaling with V_0 . From Fig. 3(b) we see that for small V_0 the polaron energy correction, $E_0 + 2t$, follows the perturbative result, $E_0 = -2t - V_0^2/\sqrt{B(B+4t)}$, independently of the value of B [44]. With increasing V_0 , however, the energy of the polaron diverges from this scaling, with the results for smaller B values deviating stronger at smaller V_0/t . This behavior originates from the fact that perturbation theory breaks down for $V_0 > 2\sqrt{Bt}$, where the rotor-electron interaction creates a large number of rotor excitations.

The fact that the ferroelectric dressing of the electron observed in Fig. 2 takes place beyond the regime of validity of perturbation theory, implies that it originates from the collective excitations of the rotor array and their coupling to the electron. Since the spectrum of rotors is different from that of harmonic oscillators, the non-perturbative physics of the ferroelectric polaron given by Eq. (1) is fundamentally distinct from the traditional polaron models such as the Holstein polaron [42, 47, 48].

The fundamental difference between the $B < 10^{-2}t$ and $B \approx t$ regimes is directly observable by comparing the polaron energies for different B 's near the crossover point at $V_0 \sim 2t$, see Fig. 3(a). For smaller $B < 10^{-2}t$ and $V_0 < 2t$, the polaron energy features an almost linear decrease according to $E_0 \approx -2t - \sqrt{2}V_0$, stemming from the strong polarization of the rotors in the vicinity of the electron at $\phi \approx 3\pi/2$. This results in the potential energy contribution $\sim V_0[\cos(3\pi/2 - \pi/4) + \cos(3\pi/2 - 3\pi/4)] = -\sqrt{2}V_0$. For stronger interactions, $V_0 > 2t$, the polaron energy decreases faster than $\propto -\sqrt{2}V_0$ due to the domain-wall formation at the electron positions, which increases the rotor-electron attraction. For larger $B \sim t$, the behaviour of the system is altered as the polaron energy decreases quadratically. This is due to the large

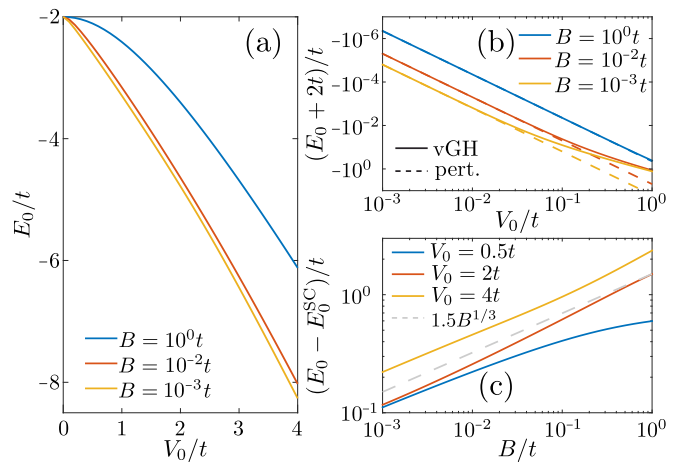


FIG. 3. (a, b) Polaron energy, E_0 , for different values of B as a function of V_0 . (b) compares the vGH results (solid lines) with perturbation theory (dashed lines). (c) B -dependence of the energy difference between the polaron energy from vGH and the related semiclassical model, $E_0 - E_0^{\text{SC}}$, for different values of V_0 . The dashed line is an eye-guide to estimate the scaling of this quantity with B (see the text). In all cases $M = 1024$.

amount of energy required to create rotor excitations which hinders their polarization and the associated potential energy benefit, thereby precluding the formation of ferroelectric order.

This latter argumentation can be made concrete by comparing the energy of our model to the semiclassical result. Let us consider a single electron within a ferroelectric domain wall of dipoles polarized at $\phi_L = 3\pi/2 - \theta$ and $\phi_R = 3\pi/2 + \theta$ on the left and right sides of the electron, respectively. Here θ parametrizes the misalignment of the domains, as described by Eq. (1) in the limit of $B = 0$. Fig. 3(c) shows that the ground state energy of this model (obtained through minimizing over θ), E_0^{SC} , is consistent with the extrapolation of the polaron energy, E_0 , for $B \rightarrow 0$. As indicated by the dashed line, $E_0 - E_0^{\text{SC}} \propto B^{1/3}$. This is consistent with the interpretation that the polaron energy exceeds the semiclassical result by the zero-point energy of the rotors, associated with a broadening of their distribution around their average angle, see Fig. 2(a). At larger B , the polaron energy diverges from this scaling, with stronger deviations for smaller V_0 . This can be attributed to the absence of ferroelectric order in the entire range of V_0 for $B \sim t$, since the rotors are more difficult to excite in this case.

Having identified the basic properties of the polaronic states and discussed their origin based on energetic arguments, let us focus on their coherence and transport properties and their relation to the effects observed in HOIP. The polaron size is associated with the extent of the ferroelectric order in the vicinity of the electron, see Fig. 2. This property can be expressed through the variance of the rotor angle, $\sigma_\phi(j) = \int d\phi_j (\phi_j - \langle \phi_j \rangle)^2 \rho^{(1)}(\phi_j)$, over the variance of the uniform distribution, $\sigma_0 = \frac{2\pi}{\sqrt{12}}$. The

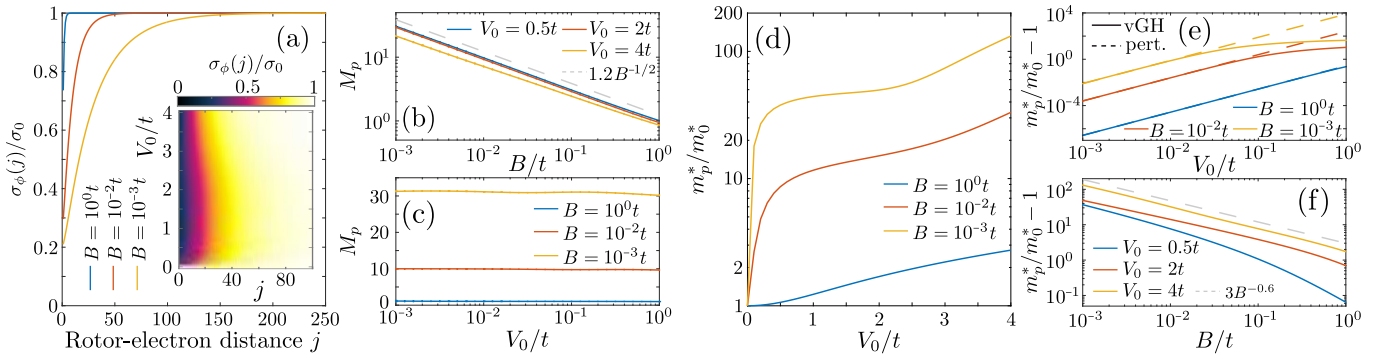


FIG. 4. (a) Variance of the rotor orientations, $\sigma_\phi(j)/\sigma_0$, for different B and $V_0/t = 0.5$. The inset shows the V_0 dependence of $\sigma_\phi(j)/\sigma_0$ for $B = 10^{-3}t$. (b, c) Polaron size estimate, M_p , derived from exponential fits of $\sigma_\phi(j)/\sigma_0$ as a function of (b) B and (c) V_0 . (d, e) The ratio of the polaron and free electron effective masses, m_p^*/m_0^* for different values of B , as a function of V_0 . (e) Compares the vGH results (solid lines) to perturbation theory (dashed lines). (f) The ratio m_p^*/m_0^* as a function of B . The dashed line in (c) and (f) serves as an eye-guide to estimate the scaling of the corresponding quantities with B . In all cases $M = 1024$.

extremal value, $\sigma_\phi(j)/\sigma_0 = 1$, corresponds to a uniform density profile, where the dipoles are unaffected by the electron motion. A smaller value, $0 \leq \sigma_\phi(j)/\sigma_0 < 1$, corresponds to the polarization of the j -th rotor typical for ferroelectric order.

The localization of ferroelectric order is demonstrated by the exponential trend of $\sigma_\phi(j)/\sigma_0$ which rapidly saturates to unity as rotors far away from the electron remain not oriented, see Fig. 4(a). For smaller B but fixed V_0 , a larger number of rotors can be excited giving rise to a more extensive dressing cloud around the electron. Inversely, the polaron for $t = B$ is very strongly localized in the vicinity of electron, $j \rightarrow 0$, and thus cannot be called a large polaron. This is fully consistent with our energetic arguments regarding E_0 , see Fig. 3(a), and is clarified further in Fig. 4(b). Here we use an exponential fit, $\sigma_\phi(j)/\sigma_0 = 1 + (\sigma_\phi(1)/\sigma_0 - 1)e^{-(j-1)/M_p}$ for $j < M/2$, to extract the polaron size M_p . This establishes that almost independently of V_0 , the size of the polaron scales as $\propto B^{-1/2}$ (thus the polaron size grows with decreasing B).

In contrast, for a constant B , the spatial extent of the polaron depends on V_0 only very weakly, see the inset of Fig. 4(a), especially within the polarized regime, $V_0 < 2t$. This observation is confirmed by Fig. 4(c), which shows that M_p is largely independent on V_0 even for very small B 's. Therefore, an overall increase of σ_ϕ/σ_0 for $V_0 \rightarrow 0$ (apparent in the inset of Fig. 4(a)), is attributed to the fact that $\sigma_\phi(1)/\sigma_0 \rightarrow 1$ due to the decreased confinement of the rotors adjacent to the electron, rather than due an actual decrease of the polaron size, M_p . For $V_0 > 2t$, where the ferroelectric domain walls form, the spatial extent of the polaron slightly decreases, see the inset of Fig. 4(a), demonstrating the shrinking tendency of the polaron in this regime.

The formation of the ferroelectric order crucially affects the polaron mobility, Fig. 4(d). Indeed, the effective mass of the polaron exhibits a strong overall in-

crease for smaller B . For $B < 10^{-2}t$ the initial growth of $m_p^* = (\partial^2 E_p / \partial q^2)^{-1}$ at smaller V_0 is followed by a plateau at $V_0 \sim t$. This can be rationalized by considering how m_p^* scales with B and V_0 . From Fig. 4(e) we see that for small V_0 the effective mass increases following the perturbative result, $m_p^*/m_0^* = 1 + V_0^2(B + 2t)/[B(B + 4t)]^{3/2}$, and saturates at larger V_0 [44]. The saturation of m_p^* can be thought of as an almost rigid attachment of the ferroelectric polarization cloud to the electron in the strongly interacting regime. For $B \sim t$ such an attachment is precluded by rapid rotation of the rotors, resulting in no saturation of m_p^* . The scaling of m_p^* with B , Fig. 4(f), demonstrates significant deviations from the perturbative result, $m_p^*/m_0^* - 1 \propto B^{-3/2}$, in the region where the ferroelectric polaron forms, $V_0 \sim t \gg B$. The B scaling is found to be significantly less steep, $m_p^*/m_0^* - 1 \propto B^{-0.6}$ for $V = 0.5t, 4t$, and $m_p^*/m_0^* - 1 \propto B^{-0.5}$, in the crossover region where $V_0 \sim 2t$. Importantly, though, m_p^* is a decreasing function of B in all of the considered cases.

Thus our $V_0 < 2t$ results show that although the polaron is large, it features low but non-negligible mobility which is consistent with HOIP experiments [31]. We would like to emphasize that the simultaneous power-law increase of the polaron size, M_p , and of its effective mass, m_p^* , with decreasing B , see Fig. 4(b, f), is the behaviour that sets our model apart from the well-known Holstein and Fröhlich polarons models, where larger effective masses are associated with smaller polaron sizes [42, 47–49] or with negligible mobilities for extremely heavy polarons [50, 51]. This indicates that the new framework of rotor lattices introduced here has the potential to explain the apparently contradicting features of carrier dynamics in HOIP.

For $V_0 > 2t$, the effective mass of the polaron grows with V_0 , Fig. 4(d), as a consequence of the reduced mobility due to the domain wall co-moving with the electron. The decrease of the polaron size with V_0 in this regime (see the inset of Fig. 4(a)) reveals the similarities between

the ferroelectric polaron and the small Holstein-like polaron once the ferroelectric domain wall is formed.

In conclusion, we have devised a minimal, tractable, and extendable rotor lattice model describing the formation of ferroelectric polarons [25–27]. This model captures several features of polarons observed in HOIP such as their low mobility but large coherence length. Furthermore, it provides an intuition for possible mechanisms leading to the formation of large polarons at ferroelectric domain boundaries, as proposed in Ref. [27]. Our model lays the groundwork for realizing a top-down approach to the carrier dynamics in HOIP, complementary to the existing density functional theory studies [17–20]. Possible extensions include studying the phase diagram of the two-dimensional lattice system where signatures of carrier localization along certain directions can be identified. The study of electron–hole interactions mediated by the rotors can elucidate the impact of the molecules on the observed long carrier lifetimes. Different forms of rotor–phonon coupling Hamiltonians can be accounted for in order to fully capture the ferroelectric properties of HOIP materials. In addition, studies that connect the abstract model parameters with realistic material properties will be crucial. The possibility of angulon formation affecting molecular mobility [52–56] and of the halogen-metal hybridization modifying the molecule-carrier interaction [57, 58] might also be relevant for reliable modeling of HOIP properties with rotor lattice setups.

We thank Artem Volosniev and Alexandra V. Zampetaki for fruitful discussions and comments. This project received funding from the European Union’s Horizon 2020 research and innovation programme under the Marie Skłodowska-Curie grant agreement No. 101034413. M.L. acknowledges support by the European Research Council (ERC) Starting Grant No. 801770 (ANGULON).

-
- [1] T. M. Brenner, D. A. Egger, L. Kronik, G. Hodes, and D. Cahen, Hybrid organic–inorganic perovskites: low-cost semiconductors with intriguing charge-transport properties, *Nat. Rev. Mater.* **1**, 1 (2016).
- [2] M. B. Johnston and L. M. Herz, Hybrid perovskites for photovoltaics: charge-carrier recombination, diffusion, and radiative efficiencies, *Acc. Chem. Res.* **49**, 146 (2016).
- [3] A. K. Jena, A. Kulkarni, and T. Miyasaka, Halide perovskite photovoltaics: background, status, and future prospects, *Chem. Rev.* **119**, 3036 (2019).
- [4] A. Kojima, K. Teshima, Y. Shirai, and T. Miyasaka, Organometal halide perovskites as visible-light sensitizers for photovoltaic cells, *J. Am. Chem. Soc.* **131**, 6050 (2009).
- [5] I. Chung, B. Lee, J. He, R. P. Chang, and M. G. Kanatzidis, All-solid-state dye-sensitized solar cells with high efficiency, *Nature* **485**, 486 (2012).
- [6] M. M. Lee, J. Teuscher, T. Miyasaka, T. N. Murakami, and H. J. Snaith, Efficient hybrid solar cells based on meso-superstructured organometal halide perovskites, *Science* **338**, 643 (2012).
- [7] H.-S. Kim, C.-R. Lee, J.-H. Im, K.-B. Lee, T. Moehl, A. Marchioro, S.-J. Moon, R. Humphry-Baker, J.-H. Yum, J. E. Moser, M. Grätzel, and N.-G. Park, Lead iodide perovskite sensitized all-solid-state submicron thin film mesoscopic solar cell with efficiency exceeding 9%, *Sci. Rep.* **2**, 1 (2012).
- [8] T. Miyasaka, *Perovskite Photovoltaics and Optoelectronics: From Fundamentals to Advanced Applications* (John Wiley & Sons, 2021).
- [9] H. Fujiwara, *Hybrid Perovskite Solar Cells: Characteristics and Operation* (John Wiley & Sons, 2022).
- [10] K. Miyata, T. L. Atallah, and X.-Y. Zhu, Lead halide perovskites: Crystal-liquid duality, phonon glass electron crystals, and large polaron formation, *Sci. Adv.* **3**, e1701469 (2017).
- [11] C. Eames, J. M. Frost, P. R. Barnes, B. C. O’regan, A. Walsh, and M. S. Islam, Ionic transport in hybrid lead iodide perovskite solar cells, *Nat. Commun.* **6**, 1 (2015).
- [12] Y. Yuan and J. Huang, Ion migration in organometal trihalide perovskite and its impact on photovoltaic efficiency and stability, *Acc. Chem. Res.* **49**, 286 (2016).
- [13] T. Chen, W.-L. Chen, B. J. Foley, J. Lee, J. P. Ruff, J. P. Ko, C. M. Brown, L. W. Harriger, D. Zhang, C. Park, M. Yoon, Y.-M. Chang, J. J. Choi, and S.-H. Lee, Origin of long lifetime of band-edge charge carriers in organic–inorganic lead iodide perovskites, *Proc. Natl. Acad. Sci. U.S.A.* **114**, 7519 (2017).
- [14] O. Selig, A. Sadhanala, C. Müller, R. Lovrincic, Z. Chen, Y. L. Rezus, J. M. Frost, T. L. Jansen, and A. A. Bakulin, Organic cation rotation and immobilization in pure and mixed methylammonium lead-halide perovskites, *J. Am. Chem. Soc.* **139**, 4068 (2017).
- [15] S. Liu, R. Guo, and F. Xie, The effects of organic cation rotation on hybrid organic-inorganic perovskites: A critical review, *Mater. Des.* **221**, 110951 (2022).
- [16] E. M. Mozur and J. R. Neilson, Cation dynamics in hybrid halide perovskites, *Annu. Rev. Mater. Res.* **51**, 269 (2021).
- [17] J. Even, L. Pedesseau, J.-M. Jancu, and C. Katan, DFT and $\mathbf{k} \cdot \mathbf{p}$ modelling of the phase transitions of lead and tin halide perovskites for photovoltaic cells, *Phys. Status Solidi RRL* **8**, 31 (2014).
- [18] J. Even, L. Pedesseau, C. Katan, M. Kepenekian, J.-S. Lauret, D. Saponi, and E. Deleporte, Solid-state physics perspective on hybrid perovskite semiconductors, *J. Phys. Chem. C* **119**, 10161 (2015).
- [19] S. Yun, X. Zhou, J. Even, and A. Hagfeldt, Theoretical treatment of $\text{CH}_3\text{NH}_3\text{PbI}_3$ perovskite solar cells, *Angew. Chem. Int. Ed. Engl.* **56**, 15806 (2017).
- [20] B. Traoré, J. Even, L. Pedesseau, M. Kepenekian, and C. Katan, Band gap, effective masses, and energy level alignment of 2D and 3D halide perovskites and heterostructures using DFT-1/2, *Phys. Rev. Mater.* **6**, 014604 (2022).
- [21] D. Meggiolaro, F. Ambrosio, E. Mosconi, A. Mahata, and F. De Angelis, Polarons in metal halide perovskites, *Adv. Energy Mater.* **10**, 1902748 (2020).
- [22] R. Jinnouchi, J. Lahnsteiner, F. Karsai, G. Kresse, and M. Bokdam, Phase transitions of hybrid perovskites simulated by machine-learning force

- fields trained on the fly with Bayesian inference, *Phys. Rev. Lett.* **122**, 225701 (2019).
- [23] L. Zhang, M. He, and S. Shao, Machine learning for halide perovskite materials, *Nano Energy* **78**, 105380 (2020).
- [24] C. W. Myung, A. Hajibabaei, J.-H. Cha, M. Ha, J. Kim, and K. S. Kim, Challenges, opportunities, and prospects in metal halide perovskites from theoretical and machine learning perspectives, *Adv. Energy Mater.* **12**, 2202279 (2022).
- [25] K. Miyata, D. Meggiolaro, M. T. Trinh, P. P. Joshi, E. Mosconi, S. C. Jones, F. De Angelis, and X.-Y. Zhu, Large polarons in lead halide perovskites, *Sci. Adv.* **3**, e1701217 (2017).
- [26] K. Miyata and X.-Y. Zhu, Ferroelectric large polarons, *Nat. Mater.* **17**, 379 (2018).
- [27] F. Wang, Y. Fu, M. E. Ziffer, Y. Dai, S. F. Maehrlein, and X.-Y. Zhu, Solvated electrons in solids—ferroelectric large polarons in lead halide perovskites, *J. Am. Chem. Soc.* **143**, 5 (2020).
- [28] J. Even, L. Pedesseau, and C. Katan, Analysis of multi-valley and multibandgap absorption and enhancement of free carriers related to exciton screening in hybrid perovskites, *J. Phys. Chem. C* **118**, 11566 (2014).
- [29] A. Amat, E. Mosconi, E. Ronca, C. Quarti, P. Umari, M. K. Nazeeruddin, M. Gratzel, and F. De Angelis, Cation-induced band-gap tuning in organohalide perovskites: interplay of spin-orbit coupling and octahedra tilting, *Nano Lett.* **14**, 3608 (2014).
- [30] F. Zheng, L. Z. Tan, S. Liu, and A. M. Rappe, Rashba spin-orbit coupling enhanced carrier lifetime in $\text{CH}_3\text{NH}_3\text{PbI}_3$, *Nano Lett.* **15**, 7794 (2015).
- [31] T. M. Brenner, D. A. Egger, A. M. Rappe, L. Kronik, G. Hodes, and D. Cahen, Are mobilities in hybrid organic-inorganic halide perovskites actually “high”?, *J. Phys. Chem. Lett.* **6**, 4754 (2015).
- [32] X.-Y. Zhu and V. Podzorov, Charge carriers in hybrid organic-inorganic lead halide perovskites might be protected as large polarons, *J. Phys. Chem. Lett.* **6**, 4758 (2015).
- [33] E. Welch, L. Scolfaro, and A. Zakhidov, Density functional theory+ u modeling of polarons in organohalide lead perovskites, *AIP Adv.* **6**, 125037 (2016).
- [34] A. J. Neukirch, W. Nie, J.-C. Blancon, K. Appavoo, H. Tsai, M. Y. Sfeir, C. Katan, L. Pedesseau, J. Even, J. J. Crochet, G. Gupta, A. D. Mohite, and S. Tretiak, Polaron stabilization by cooperative lattice distortion and cation rotations in hybrid perovskite materials, *Nano Lett.* **16**, 3809 (2016).
- [35] T. Ivanovska, C. Dionigi, E. Mosconi, F. De Angelis, F. Liscio, V. Morandi, and G. Ruani, Long-lived photoinduced polarons in organohalide perovskites, *J. Phys. Chem. Lett.* **8**, 3081 (2017).
- [36] F. Zheng and L.-w. Wang, Large polaron formation and its effect on electron transport in hybrid perovskites, *Energy Environ. Sci.* **12**, 1219 (2019).
- [37] F. Ambrosio, J. Wiktor, F. De Angelis, and A. Pasquarello, Origin of low electron-hole recombination rate in metal halide perovskites, *Energy Environ. Sci.* **11**, 101 (2018).
- [38] F. Ambrosio, D. Meggiolaro, E. Mosconi, and F. De Angelis, Charge localization, stabilization, and hopping in lead halide perovskites: competition between polaron stabilization and cation disorder, *ACS Energy Lett.* **4**, 2013 (2019).
- [39] F. Wang, W. Chu, L. Huber, T. Tu, Y. Dai, J. Wang, H. Peng, J. Zhao, and X.-Y. Zhu, Phonon signatures for polaron formation in an anharmonic semiconductor, *Proc. Natl. Acad. Sci. U.S.A.* **119**, e2122436119 (2022).
- [40] H. Zhu, K. Miyata, Y. Fu, J. Wang, P. P. Joshi, D. Niesner, K. W. Williams, S. Jin, and X.-Y. Zhu, Screening in crystalline liquids protects energetic carriers in hybrid perovskites, *Science* **353**, 1409 (2016).
- [41] J. Kang and L.-W. Wang, Dynamic disorder and potential fluctuation in two-dimensional perovskite, *J. Phys. Chem. Lett.* **8**, 3875 (2017).
- [42] A. S. Alexandrov and J. T. Devreese, *Advances in Polaron Physics* (Springer, Berlin Heidelberg, , 2010).
- [43] I. G. Lang and Y. A. Firsov, Mobility of small-radius polarons at low temperatures, *Zh. Eksp. Teor. Fiz.* **45**, 378 (1963), [*Sov. Phys. JETP* **18**, 262 (1964)].
- [44] See Supplemental Material for details.
- [45] H. Spohn, Roughening and pinning transitions for the polaron, *J. Phys. A* **19**, 533 (1986).
- [46] B. Gerlach and H. Löwen, Analytical properties of polaron systems or: Do polaronic phase transitions exist or not?, *Rev. Mod. Phys.* **63**, 63 (1991).
- [47] T. Holstein, Studies of polaron motion: Part I. the molecular-crystal model, *Ann. Phys.* **8**, 325 (1959).
- [48] T. Holstein, Studies of polaron motion: Part II. the “small” polaron, *Ann. Phys.* **8**, 343 (1959).
- [49] E. Jeckelmann and S. R. White, Density-matrix renormalization-group study of the polaron problem in the Holstein model, *Phys. Rev. B* **57**, 6376 (1998).
- [50] A. S. Alexandrov and B. Y. Yavidov, Small adiabatic polaron with a long-range electron-phonon interaction, *Phys. Rev. B* **69**, 073101 (2004).
- [51] O. R. Tozer and W. Barford, Localization of large polarons in the disordered Holstein model, *Phys. Rev. B* **89**, 155434 (2014).
- [52] R. Schmidt and M. Lemesko, Rotation of quantum impurities in the presence of a many-body environment, *Phys. Rev. Lett.* **114**, 203001 (2015).
- [53] R. Schmidt and M. Lemesko, Deformation of a quantum many-particle system by a rotating impurity, *Phys. Rev. X* **6**, 011012 (2016).
- [54] E. Yakaboylu and M. Lemesko, Anomalous screening of quantum impurities by a neutral environment, *Phys. Rev. Lett.* **118**, 085302 (2017).
- [55] Y. Cui, Y.-Y. Liu, J.-P. Deng, X.-Z. Zhang, R.-B. Yang, Z.-Q. Li, and Z.-W. Wang, Microscopic theory of raman scattering for the rotational organic cation in metal halide perovskites, arXiv:2209.13861 (2022).
- [56] J.-W. Wu, Y. Cui, S.-J. Li, and Z.-W. Wang, Optical absorption of angulon in metal halide perovskites, arXiv:2212.06356 (2022).
- [57] A. G. Volosniev, A. S. Kumar, D. Lorenc, Y. Ashourishokri, A. A. Zhumekenov, O. M. Bakr, M. Lemesko, and Z. Alpichshev, Spin-electric coupling in lead-halide perovskites, *Phys. Rev. Lett.*, in press, arXiv:2203.09443 (2023).
- [58] A. G. Volosniev, A. S. Kumar, D. Lorenc, Y. Ashourishokri, A. A. Zhumekenov, O. M. Bakr, M. Lemesko, and Z. Alpichshev, Effective model for studying optical properties of lead-halide perovskites, *Phys. Rev. B.*, in press, arXiv:2204.04022 (2023).